



Phase-detection probe measurements in high-velocity free-surface flows including a discussion of key sampling parameters



Stefan Felder^{a,*}, Hubert Chanson^b

^a Water Research Laboratory, School of Civil and Environmental Engineering, UNSW Australia, Manly Vale, NSW 2093, Australia

^b School of Civil Engineering, The University of Queensland, Brisbane, QLD 4072, Australia

ARTICLE INFO

Article history:

Received 22 July 2014

Received in revised form 29 September 2014

Accepted 10 October 2014

Available online 28 October 2014

Keywords:

Conductivity probes

Signal processing

Stepped spillway

Air–water flow properties

Transition flows

Sampling parameters

ABSTRACT

Air–water high-velocity flows are characterised by strong interactions of air bubbles and water droplets. The void fraction ranges from a few percent in bubbly flows to up to 100% at the free-surface and a reliable measurement instrumentation is the phase-detection intrusive probe. Herein new experiments were conducted on a stepped spillway ($\theta = 26.6^\circ$) in transition and skimming flow sub-regimes yielding new insights into the turbulent air–water flow properties including the turbulence intensities and integral turbulent time and length scales. The integral turbulent scales showed self-similarity independently of the flow regime. A sensitivity analysis was conducted on the phase-detection probe signals to investigate the optimum sampling duration and frequency as well as the data analysis parameters threshold, sub-sampling duration, histogram bin sizes and cut-off effects. The results provide recommendations in terms of optimum sampling and processing parameters for high-velocity air–water flows.

© 2014 Elsevier Inc. All rights reserved.

1. Introduction

High-velocity self-aerated flows are often called “white waters” because of the entrained air [45,52,15]. The free-surface aeration in high-velocity open channel flows induces a drastic change in the multiphase (gas–liquid) flow structure and its distribution within the water column that have direct implications in terms of bubble–turbulence interactions and associated turbulent mixing processes [4,19]. Most high-velocity free-surface flows are characterised by large amounts of entrained air. The void fractions range from a few percents to nearly 100% in the upper spray region, and the ratios of flow velocity to bubble rise velocity are commonly greater than 10–20.

Classical measurement techniques are adversely affected by the presence of air bubbles and air–water interfaces, and they can produce highly inaccurate readings: e.g., pointer gauge, Pitot tube, acoustic Doppler velocimeter (ADV), laser Doppler anemometer (LDA), particle image velocimetry (PIV) [37,19]. Many air–water flow measurement techniques are available depending upon flow type and void fraction fractions (Boyer et al. [5]). For low void

fractions, a phase Doppler anemometer (PDA) may provide some meaningful results in terms of turbulence properties and bubble characteristics [51]. When the void fraction C , or liquid fraction $(1 - C)$, exceeds about 1–3%, the most reliable metrology is the intrusive phase detection probes, notably the optical fibre probe and conductivity/resistivity probe [11,2,16]. The principle behind the optical fibre probe is a change in optical index between the two phases [10,12,41]. The conductivity/electrical probe works based upon the difference in electrical resistivity between air and water [33,47]. Phase-detection intrusive probes are designed to pierce bubbles and droplets and their design is typically based upon the needle probe design developed by Neal and Bankoff [42], Neal and Bankoff [43]. Such probes have been used for over 50 years, including some milestone prototype measurements on the Aviemore Dam spillway in New Zealand [7,8].

High-velocity free-surface flows are typical on spillways with slopes ranging between very flat ($\theta = 3^\circ$) to very steep ($\theta = 60^\circ$). Spillways may be constructed with smooth surface or roughened surface such as rockfill or step elements. An advantageous spillways design is the stepped spillway which provides a stronger air entrainment and energy dissipation performances compared to smooth chutes because the large roughness steps increase the flow resistance. Many experimental studies of stepped spillway flows have been conducted in the last decades for steeply sloped stepped chutes [13,3,39,31] and with embankment dam slopes (e.g. [50,20,6,36,29]). While previous studies provided extensive

* Corresponding author. Tel.: +61 2 8071 9861.

E-mail addresses: s.felder@unsw.edu.au (S. Felder), h.chanson@uq.edu.au (H. Chanson).

¹ Formerly: School of Civil Engineering, The University of Queensland, Brisbane, QLD 4072, Australia.

insights into the flow processes at design discharge in the skimming flow regime, little information is available about the air–water flow properties for transition flow discharges apart from a few studies [23,26]. The transition flow regime occurs for intermediate flow rates and hence an inclusive analysis of both transition and skimming flow properties is missing. Herein new experiments were conducted in high-velocity free-surface flows on a large scale stepped spillway model with a slope of $\theta = 26.6^\circ$ comprising both flow regimes. The experiments were conducted with phase-detection intrusive conductivity probes and new results for the transition flow regime include the turbulent air–water flow properties.

As part of the stepped spillway experiments, the limitations and potentials of the phase-detection conductivity probes were investigated to identify optimum sampling parameters. Despite some key contributions [10,16,20], the use of phase-detection probes in high-velocity free-surface flows is restricted by a lack of accurate method to select the optimum sampling parameters, albeit for a few sensitivity analysis for basic air–water flow properties [50,1]. Herein a sensitivity analysis of air–water flow data was conducted to investigate systematically the effects of the sampling duration, sampling frequency and sub-sampling duration on the turbulent air–water flow properties. Furthermore the effects of the air–water threshold, the histogram bin sizes for the voltage signals and the cut-off effect on the lower voltage signals were tested. A procedure for phase-detection probe measurements in high-velocity self-aerated flows is discussed.

2. Instrumentation and signal processing

Phase-detection intrusive probes were used for the measurements of air–water interfaces in the aerated free-surface flows. Two probe configurations were used. A double-tip conductivity probe comprised two identical sensors separated by a streamwise distance $\Delta x = 7.2$ mm (Fig. 1A). Fig. 1A illustrates such a double-tip designed to pierce the air bubbles and water droplets in the mainstream flow direction. The double-tip conductivity probe was used for a detailed sensitivity analysis of sampling parameters in air–water flows. The second configuration comprised two single-tip needle probes separated by a transverse distance Δz (Fig. 1B). A similar probe configuration has been also used by Chanson and Carosi [21], Felder and Chanson [28].

The measurement of the air–water interfaces is an Eulerian observation of air bubbles and water droplets at a fixed location within the air–water flows over a specific sampling duration. At that location, the air bubbles and water droplets are detected when they pierced the probe tips. This results in a square wave voltage signal as illustrated in Fig. 2. In Fig. 2A, a voltage signal of about 4 indicates the probe tip in water and a voltage of 0.5 is equivalent to an air voltage. The raw signal is not squared and therefore a signal processing technique must be used to identify the air and water voltages. Fig. 2B illustrates the PDF of the raw voltage signals with bin sizes of 0.1 V for the data shown in Fig. 2A. For this data set, the amount of air and water is close and two distinctive voltage peaks are visible indicating air and water voltages. Different types of processing techniques have been used to identify the air–water phases and good overviews were given by Cartellier and Achard [11], Toombes [50]. Two classes of processing techniques are common. One is based upon threshold criteria derived from the PDF of the raw voltage signals and another identifies air and water phases according to a change in slope of the raw voltage signal.

Herein a simple (single) threshold technique was used to analyse the raw voltage signals and to calculate the basic air–water flow properties including void fraction and bubble count rate. The single threshold technique is robust. It is best suited to cover the wide range of void fractions in the whole air–water flow

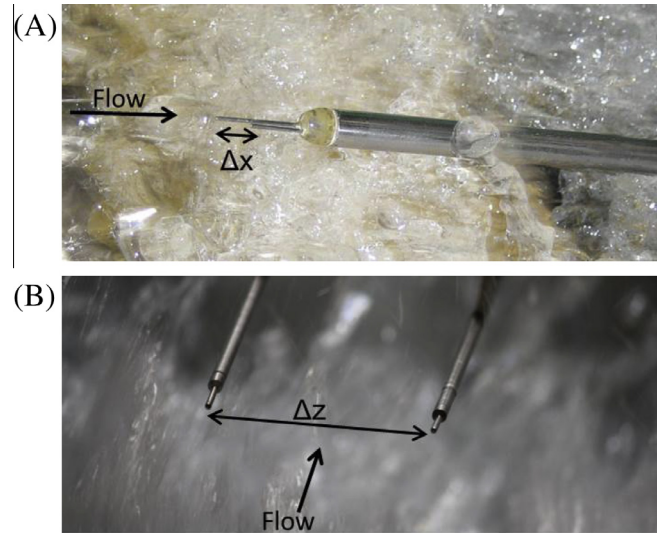


Fig. 1. Conductivity probe designs developed at the University of Queensland. (A) Double-tip probe ($\varnothing = 0.25$ mm, $\Delta x = 7.2$ mm, $\Delta z = 2.1$ mm) – view in elevation. (B) Single-tip probes ($\varnothing = 0.35$ mm, $\Delta x = 0$ mm, $\Delta z = 50.7$ mm).

column. The single threshold technique can identify the instantaneous void fraction $c = 1$ in air and $c = 0$ in water. The instantaneous void fraction may be used to calculate the time-averaged void fraction, the bubble count rate, the air/water chord times, the bubble/droplet chord lengths and the streamwise particle grouping. In the present study, the instantaneous void fraction was used to quantify the time the probe tip was in air and to calculate the time-averaged void fraction:

$$C = \frac{\sum_{i=1}^n c}{n} \quad (1)$$

where n is the number of samples. The calculation of the bubble count rate was based upon the number of water to air interfaces. The air bubble and water droplet chord times were defined as the time between air to water and water to air interfaces respectively and the multiplication with the local velocity provided the air bubble and water droplet chord lengths. The chord sizes were not the bubble diameters, but characteristic streamwise air–water sizes [22].

The calculation of further air–water flow properties is based upon statistical analyses of the raw Voltage signals. A cross-correlation between the two 2-tip probe sensor signals provides the cross-correlation function and the maximum cross-correlation coefficient $(R_{xy})_{\max}$ [35,15,24]. The ratio of the sensor separation Δx to the transit time T of the maximum cross-correlation gives the local time-averaged interfacial velocity:

$$V = \frac{\Delta x}{T} \quad (2)$$

The broadening of the cross-correlation function compared to the auto-correlation function of the leading sensor may provide some information about the turbulence intensities in an air–water flow [38,16]. Chanson and Toombes [22] derived an equation for a dimensionless expression of the turbulence velocity fluctuations:

$$Tu = 0.851 \times \frac{\sqrt{\tau_{0.5}^2 - T_{0.5}^2}}{T} \quad (3)$$

where $\tau_{0.5}$ is the time scale for which the cross-correlation function is half of its maximum value such as: $R_{xy}(T + \tau_{0.5}) = 0.5 \times R_{xy}(T)$, and $T_{0.5}$ is the characteristic time for which the normalised auto-correlation function equals: $R_{xx}(T_{0.5}) = 0.5$.

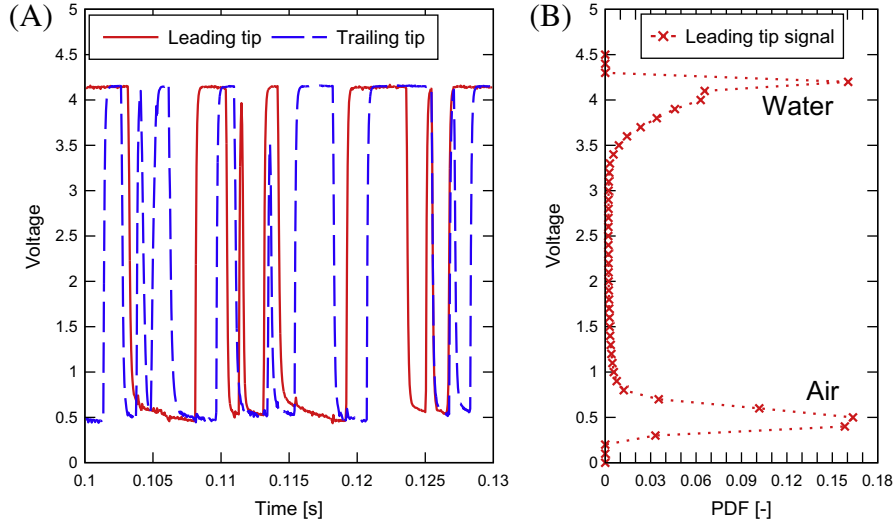


Fig. 2. Voltage signal of a double-tip conductivity probe in a high-velocity skimming flows on a stepped spillway in the intermediate flow region ($C = 0.48$, $F = 162.7$ Hz, $V = 3.7$ m/s). (A) Raw signal of double-tip conductivity probe. (B) PDF of voltage signal.

The integration of the auto- and cross-correlation functions from the maximum correlation till the first zero-crossing of the correlation curve yields the integral time scales T_{xx} and T_{xy} :

$$T_{xx} = \int_{\tau=0}^{\tau=\tau(R_{xx}=0)} R_{xx}(\tau) \times d\tau \quad (4)$$

$$T_{xy} = \int_{\tau=\tau(R_{xy}=(R_{xy})_{\max})}^{\tau=\tau(R_{xy}=0)} R_{xy}(\tau) \times d\tau \quad (5)$$

T_{xx} is the auto-correlation integral time scale which characterises the longitudinal air–water flow structure [20], i.e. it represents a rough measure of the longest longitudinal connection. The cross-correlation integral time scale T_{xy} characterises the vortices advecting the air–water flow structure and is a function of the probe separation distance. [30] redefined Eq. (3) by linking the integral auto- and cross-correlation time scales to the turbulence intensity.

For the configuration with an array of two needle probes, a correlation analysis between the two sensors and the integration in transverse direction provided further information about the large advecting vortices in transverse direction. An integration of the results for different transverse separations Δz yields the transverse integral turbulent length scale:

$$L_{xz} = \int_{z=0}^{z=Z((R_{xz})_{\max}=0)} (R_{xz})_{\max} \times dz \quad (6)$$

where $(R_{xz})_{\max}$ is the maximum cross-correlation values. L_{xz} represents a characteristic dimension of the transverse integral turbulent length scale of the large vortical structures advecting the air bubbles and air–water packets [17,20].

The corresponding integral turbulent time scale is:

$$T_{\text{int}} = \frac{\int_{z=0}^{z=Z((R_{xz})_{\max}=0)} (R_{xz})_{\max} \times T_{xz} \times dz}{L_{xz}} \quad (7)$$

where T_{xz} is the transverse cross-correlation integral time scale calculated in analogy to Eq. (5).

The experiments were conducted with fast-response electronics coupled with a high-speed data acquisition system to minimize the probe response time. The response time was not affected by underestimation of bubble transit time as shown in a detailed study by Cummings [25]. In this study, the comparison of photographic technique and phase-detection intrusive probes showed a good

agreement. Cummings [25] tested also the accuracy of void fraction and velocity measurements against the measured water discharge via continuity showing accuracies of 5%. Additional tests were conducted by Carosi and Chanson [9] on the same spillway facility and by Murzyn and Chanson [40] in a hydraulic jump with the same phase-detection probes and the same acquisition system as used in the present study.

The accuracies in terms of water discharge can be estimated as about 2% and the positioning of the conductivity probes in vertical position within the spillway test section as less than 0.5 mm. The void fractions were measured with an accuracy of about $\Delta C/C = 4\%$ and the interfacial velocities had an accuracy of about $\Delta V/V = 5\%$ ($0 < C < 0.95$) and 10% for $C > 0.95$ and $C < 0.05$. The error on the bubble frequency can be estimated as $\Delta F/F = 0.5\%$.

3. Air–water flow experiments on a stepped spillway in transition and skimming flows

Air–water flow experiments were performed in a large size stepped spillway model with slope of $\theta = 26.6^\circ$ and 10 steps with height $h = 0.10$ m (Fig. 3). The spillway had a width of 1 m. A pump provided the discharge in the circuit system with an accuracy of 2% over a broad-crested weir at the upstream end of the stepped section. The experimental facility was used previously in air–water

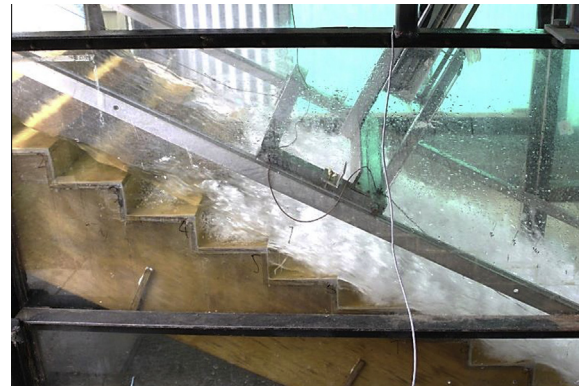


Fig. 3. Transition flow regime on the stepped spillway ($\theta = 26.6^\circ$): $d_c/h = 0.83$, $q_w = 0.075$ m²/s, $Re = 3.0 \times 10^5$.

flow studies on stepped spillways [21,28]. The experiments were conducted for a range of discharges per unit width $0.009 \leq q_w \leq 0.241 \text{ m}^2/\text{s}$ representing Reynolds numbers of $3.5 \times 10^4 \leq Re \leq 9.6 \times 10^5$. The discharges corresponded to a dimensionless flow rate $0.2 \leq d_c/h \leq 1.81$, where d_c is the critical flow depth.

Air–water flow measurements were conducted with a double-tip conductivity probe ($\varnothing = 0.25 \text{ mm}$) and the two single-tip probes (0.35 mm) using the sampling parameters identified in the sensitivity analysis (Section 4), i.e. sampling frequency 20 kHz , sampling duration 45 s , sub-sample duration 3 s , PDF bin size 0.1 V , 50% single threshold. Experiments were performed in both transition (TRA) and skimming (SK) flow sub regimes. The transition flows were observed for dimensionless flow rates of $0.69 \leq d_c/h \leq 1.0$ and the skimming flow measurements comprised flow rates of $1.0 \leq d_c/h \leq 1.74$. In these flow regimes, the flow aeration started naturally at the inception point of free-surface aeration when the turbulence velocity fluctuations close to the free-surface were strong enough to overcome buoyancy forces and free-surface tension. Downstream of the inception point, strong turbulent interactions took place between air–water interfaces

and a large proportion of the flow energy was dissipated. Fig. 3 illustrates a typical appearance of the air–water flows on the stepped spillway model for a transition flow regime. In transition flows, the flow pattern is irregular with strong droplet splashing and flapping mechanisms of air pockets in the step niches (Fig. 3) [23]. For the larger discharges in skimming flows, the flow is more stable and the free-surface appears almost parallel to the pseudo-bottom formed by the step edges [46]. The air–water flow experiments were conducted in both flow regimes to investigate the air–water flow properties for a comprehensive range of flow conditions in two sub-regimes.

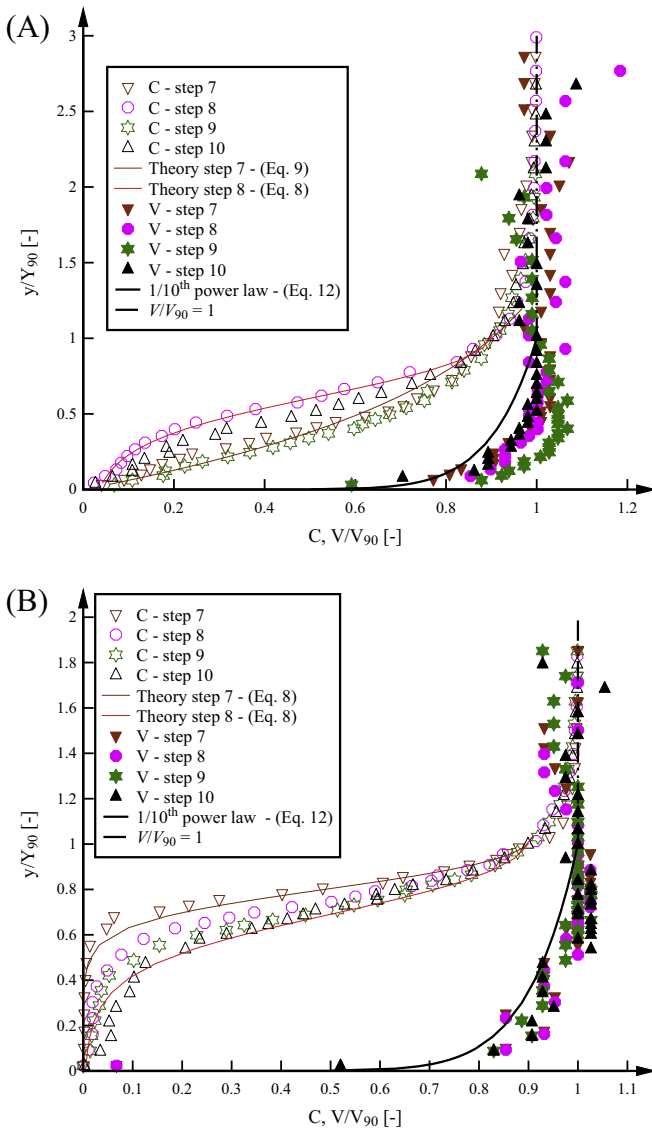


Fig. 4. Void fraction and interfacial velocity distributions; comparison with advective diffusion equation (Eqs. (8) and (9)) and power law (Eq. (12)). (A) Transition flow data: $d_c/h = 0.69$, $q_w = 0.056 \text{ m}^2/\text{s}$, $Re = 2.2 \times 10^5$. (B) Skimming flow data: $d_c/h = 1.38$, $q_w = 0.161 \text{ m}^2/\text{s}$, $Re = 6.4 \times 10^5$.

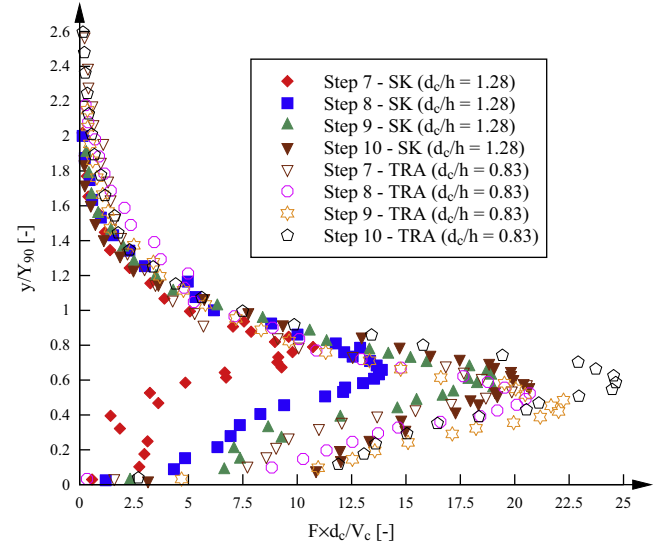


Fig. 5. Bubble count rate distributions in transition ($d_c/h = 0.83$, $q_w = 0.075 \text{ m}^2/\text{s}$, $Re = 3.0 \times 10^5$) and skimming flows ($d_c/h = 1.28$, $q_w = 0.143 \text{ m}^2/\text{s}$, $Re = 5.7 \times 10^5$).

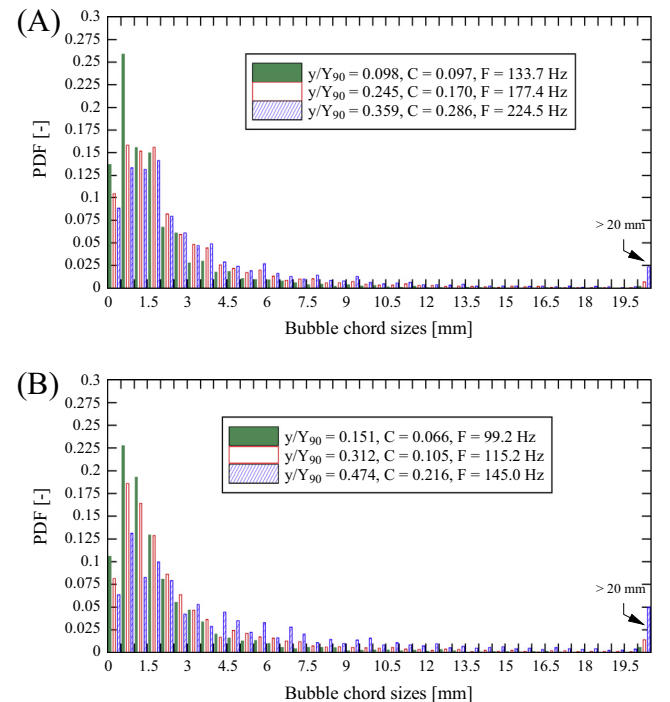


Fig. 6. Probability distribution functions of air bubble chord sizes in transition and skimming flows. (A) TRA: $d_c/h = 0.83$, $q_w = 0.075 \text{ m}^2/\text{s}$, $Re = 3.0 \times 10^5$; $h = 10 \text{ cm}$, step edge 9. (B) SK: $d_c/h = 1.29$, $q_w = 0.144 \text{ m}^2/\text{s}$, $Re = 5.7 \times 10^5$; $h = 10 \text{ cm}$, step edge 10.

3.1. Basic air–water flow properties

A key property in air–water flows is the void fraction which is the time-averaged air concentration at each measurement location. Typical distributions of void fraction at several consecutive step edges are shown in Fig. 4 as function of the dimensionless distance perpendicular to the pseudo-bottom y/Y_{90} with Y_{90} the flow depth where $C = 0.9$. For the transition flow, two different types of void fraction distributions were observed: some step edges showed flat, straight void fraction profiles and others showed S-shape distributions (Fig. 4A). These two profile types differed between adjacent step edges. The S-shape profiles followed the advective diffusion equation for air bubbles in skimming flows [22]:

$$C = 1 - \tanh^2 \left(K' - \frac{y/Y_{90}}{2 \times D_0} + \frac{(y/Y_{90} - 1/3)^3}{3 \times D_0} \right) \quad (8)$$

where K' is an integration constant and D_0 is a function of the mean air concentration C_{mean} only. Eq. (8) is added for one step edge in Fig. 4A. The flat straight void fraction profiles were similar to air concentration distributions in jets and were best compared to an analytical solution of the advective diffusion equation for transition flow [23]:

$$C = K'' \times \left(1 - \exp \left(-\lambda \times \frac{y}{Y_{90}} \right) \right) \quad (9)$$

where K'' and λ are functions of C_{mean} only:

$$C_{\text{mean}} = K'' - \frac{0.9}{\lambda} \quad (10)$$

$$K'' = \frac{0.9}{1 - e^{-\lambda}} \quad (11)$$

Eq. (9) is valid for $C_{\text{mean}} > 0.45$ [23] and added for one step edge with a flat straight void fraction profile (Fig. 4A).

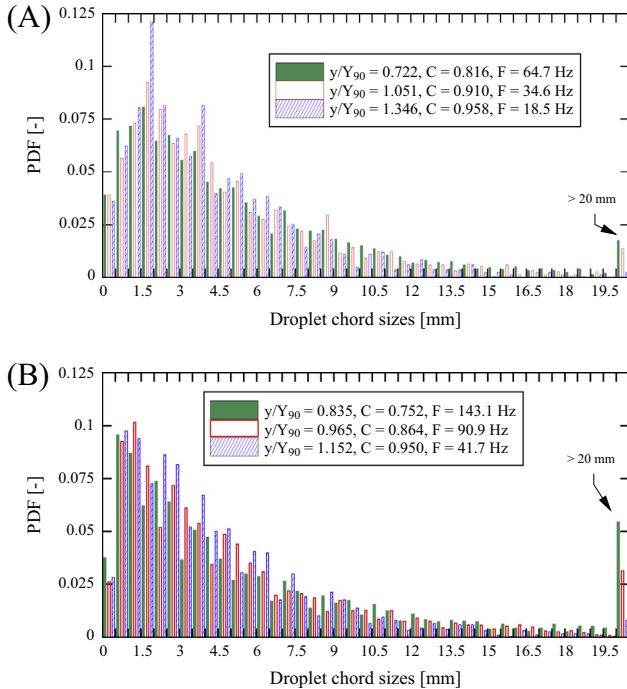


Fig. 7. Probability distribution functions of water droplet chord sizes in transition and skimming flows. (A) TRA: $d_c/h = 0.7$, $q_w = 0.020 \text{ m}^2/\text{s}$, $Re = 8.1 \times 10^4$; $h = 5 \text{ cm}$, step edge 10. (B) SK: $d_c/h = 1.49$, $q_w = 0.180 \text{ m}^2/\text{s}$, $Re = 7.2 \times 10^5$; $h = 10 \text{ cm}$, step edge 10.

The skimming flow data showed typical S-shape profiles (Fig. 4B) and compared well with Eq. (8). The present data confirmed the previous advective diffusion models for both transition and skimming flows. However the alternation of two differing profiles for transition flows confirms the instabilities of the flow regime and highlights the difficulty to predict the void fraction distributions within the flow. Indeed the flow may change from one step edge to the next (Fig. 4A).

The measurements of the time-averaged interfacial velocity were conducted with the double-tip conductivity probe and Fig. 4 illustrates the results of the dimensionless interfacial velocity V/V_{90} distributions as a function of y/Y_{90} where V_{90} is the characteristic interfacial velocity where $C = 0.9$. The skimming flow data were well correlated with a power law (Fig. 4B), commonly observed for velocity profiles in spillway flows:

$$\frac{V}{V_{90}} = \left(\frac{y}{Y_{90}} \right)^{1/N} \quad 0 \leq y/Y_{90} \leq 1 \quad (12)$$

In Eq. (12), N was typically $N = 10$ for skimming flows (e.g. [22,21,28], although other researchers found slightly different values (e.g. [3,48]). The value of N may vary from one step edge

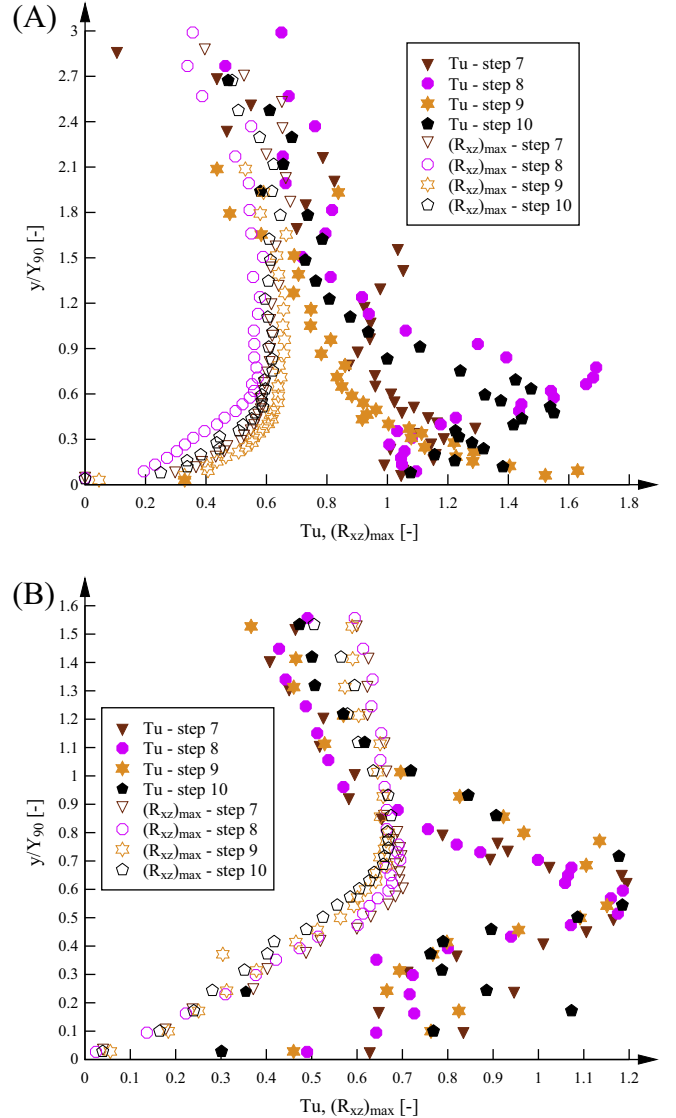


Fig. 8. Turbulence intensity and maximum cross-correlation coefficient distributions. (A) Transition flow data: $d_c/h = 0.69$, $q_w = 0.056 \text{ m}^2/\text{s}$, $Re = 2.2 \times 10^5$. (B) Skimming flow data: $d_c/h = 1.11$, $q_w = 0.116 \text{ m}^2/\text{s}$, $Re = 4.6 \times 10^5$.

to the next one for a given flow rate. For locations $y/Y_{90} > 1$ small scatter of the data was observed (Fig. 4B), but overall a uniform velocity profile fitted well the experimental data:

In the transition flow regime, the dimensionless velocity profiles showed differences in the region close to the step edge ($0 < y/Y_{90} < 0.75$) (Fig. 4A). For void fractions of about 20–50%, a bulk in velocity was observed with maxima of about $V/V_{90} \approx 1.05$. These velocity profiles were observed for step edges with straight flat void fraction profiles and seemed to be linked with the impact of air–water flows on the step edge. The interfacial velocity distributions were similar to observations in the impact region of a stepped spillway device [14] and in the region immediately downstream of the nappe impact in a nappe flow regime [50]. Furthermore similarities were seen with the findings of Pagliara et al. [44], who observed larger velocities in the region close to the end of block ramp elements. The data in the present study differed from observations of Chanson and Toombes [23] who found a best fit correlation between V/V_{\max} and y/Y_{90} for the transition flow regime for channel slopes between 3.4° and 21.8° .

The air–water interactions within the flows can be measured by the number of air–water interfaces measured as bubble count rate

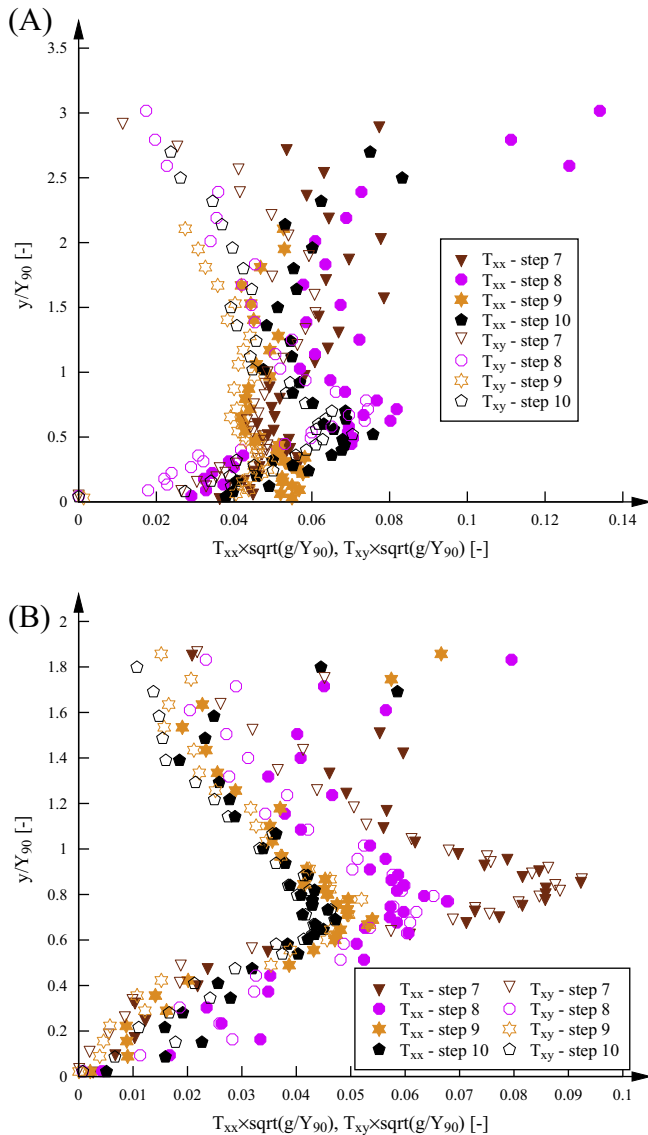


Fig. 9. Auto- and cross-correlation time scale distributions. (A) Transition flow data: $d_c/h = 0.69$, $q_w = 0.056 \text{ m}^2/\text{s}$, $Re = 2.2 \times 10^5$. (B) Skimming flow data: $d_c/h = 1.38$, $q_w = 0.161 \text{ m}^2/\text{s}$, $Re = 6.4 \times 10^5$.

F . Typical dimensionless bubble count rate distributions $F \times d_c/V_c$ are illustrated in Fig. 5 for both transition and skimming flows where d_c and V_c are the critical flow depth and critical flow velocity respectively. Little difference was observed for the two flow regimes and for all experiments, the maximum bubble count rates were observed in the intermediate flow region with void fractions between 35% and 65%. With increasing distance from the inception point of air entrainment, the overall number of entrained air bubbles increased. The observations were consistent with previous studies on stepped spillways with slopes $3.4^\circ \leq \theta \leq 30^\circ$ (e.g. [50,21,26]).

The air–water interfaces also provided microscopic information about the chord sizes of the air bubbles and water droplets in streamwise direction. The chord sizes were not the bubble diameters, but characteristic streamwise air/water sizes. For all transition and skimming flow data, the air bubble chord sizes were observed in the bubbly flow region ($C < 0.3$) and the water droplet chords in the spray region ($C > 0.7$). The distributions in both bubbly and spray flow regions and for both flow regimes showed a wide range of bubble/droplet chord sizes at each location (Figs. 6 and 7). Fig. 6 shows examples of probability distribution functions for the air bubble chord lengths for both transition and skimming flows and Fig. 7 illustrates typical results for the water droplet chord lengths. The spectrum of both bubble and droplet chord lengths ranged from less than 0.3 mm to more than 20 mm. Both the bubble and droplet chord size distributions were skewed with a preponderance of small bubbles/droplets.

The PDF of bubble chord sizes tended to follow a log-normal distribution with a mode between 0.5 and 3.0 mm (Fig. 6). The droplet chord size probability distribution functions were flatter and broader than those of the bubble chords, and tended also to follow a log-normal distribution (Fig. 7). The trends were observed for all data in the present study and the results were consistent with results of earlier skimming flow studies [22,49,21,28,29]. No major difference was observed between transition and skimming flow chord sizes.

3.2. Turbulent air–water flow properties

Turbulent air–water flow properties were calculated based upon the conductivity probe raw data as outlined in Section 2. Turbulent data have been recently presented for air–water

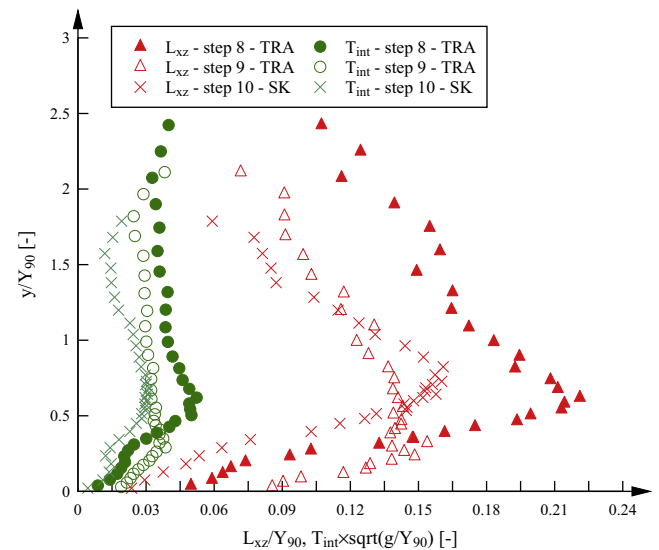


Fig. 10. Integral turbulent time and length scale distributions in transition flows: $d_c/h = 0.69$, $q_w = 0.056 \text{ m}^2/\text{s}$, $Re = 2.2 \times 10^5$ and skimming flows: $d_c/h = 1.38$, $q_w = 0.161 \text{ m}^2/\text{s}$, $Re = 6.4 \times 10^5$.

skimming flows [21,28] but not yet for the transition flow regime. Herein the present study provided the first comprehensive data set for both flow regimes.

The turbulence intensity Tu was calculated based upon the shape of the cross-correlation functions between the two probe sensor signals (Eq. (3)). For most transition and skimming flow experiments, typical turbulence intensity distributions were observed with largest turbulence levels in the intermediate flow region for void fractions between 30% and 55% and the turbulence levels were larger for the transition flow regime (Fig. 8). In transition flows, for some step edges, large turbulence levels were observed close to the step edge (Fig. 8A) which was associated with flat straight void fraction profiles. The turbulence data reflect the instabilities of the transition flow regime including the irregular impacts of the air–water flows on every second step edge as well as the irregular flapping mechanisms in the step cavities. Similar shapes of turbulence intensity distributions were reported by Felder and Chanson [28] at every second step edge on a stepped spillway with $\theta = 21.8^\circ$ in a skimming flow. For the present skimming flow discharges, most turbulence data in the bubbly flow region ($C < 30\%$) and the (upper) spray region ($y/Y_{90} > 1.5$), tended to values of about 20–50% (Fig. 8B). Fig. 8 illustrates further the maximum cross-correlation coefficients for both flow regimes. Little difference was observed for all data sets independent from the distance downstream of the inception point of air entrainment and the flow rates (Fig. 8).

The auto- and cross-correlation time scales were calculated for all data. The auto-correlation time scale T_{xx} characterised the time scale of the large eddies advecting air–water interfaces in the streamwise direction and the cross-correlation time scales T_{xy} characterised the vortices advecting the air–water flow structure (Fig. 9).

For the transition flows, good agreement was observed between the auto- and cross-correlation data and larger auto-correlation time scales were observed in the (upper) spray region which did not interact with the rest of the flow. The data showed strong scatter and differences in the distributions were visible for flat straight void fraction profiles (Fig. 9A).

For the skimming flow regime, the dimensionless distributions of T_{xx} and T_{xy} showed maximum values in the intermediate flow region with void fractions of 40–75%. In the bubbly flow region,

the time scales tended to zero (Fig. 9B). Overall the time scales for the skimming flow data were in close agreement apart from the upper spray region.

Further measurements were conducted with an array of two simultaneously sampled single-tip conductivity probes with various transverse distances $3.3 \leq \Delta z \leq 80.8$ mm. A cross-correlation analysis was performed between the signals leading the maximum transverse cross-correlation coefficient and the transverse cross-correlation time scale. Based on these values the integral turbulent length and time scales were calculated with Eqs. (6) and (7). Characteristic dimensionless results are presented in Fig. 10 as functions of y/Y_{90} for both flow regimes.

For the transition flow data, the largest integral turbulent time and length scales were observed in the intermediate flow region for void fractions between 50% and 70%. In the bubbly flow region, the turbulent scales tended to zero ($C = 0$). Small differences were observed for the two adjacent step edges and the integral turbulent scales were consistently larger for step edge 8, which was characterised by an S-shape void fraction profile. The results for the transition flow data showed similar shapes compared to the skimming flow observations and the results were consistent with features that were reported in previous studies of integral turbulent scales on stepped spillways [21,28,26].

The characteristic maximum values of integral turbulent time and length scales and advection turbulent length scales are summarised in Table 1 in dimensional and dimensionless form. The present observations are compared with previous data sets on the same stepped spillway facility with $\theta = 21.8^\circ$ [21,28] and further data on a stepped spillway with $\theta = 26.6^\circ$ with different step height and channel width respectively [26]. The characteristic maximum turbulent scales were in good agreement for all data sets (Table 1). The sizes of the large advecting eddies in transverse and longitudinal direction were mostly independent of step heights and of channel slopes, but scale effects are an issue as shown by Felder and Chanson [28] for $\theta = 21.8^\circ$ and by Felder [26] for $\theta = 26.6^\circ$.

Felder and Chanson [27] found self-similar relationships between void fraction and dimensionless integral turbulent time and length scales respectively best reflected with a skewed parabolic shape. The correlation was developed for stepped spillway data with $\theta = 21.8^\circ$ and with $h = 5$ cm and $h = 10$ cm:

Table 1
Summary of characteristic transverse integral turbulent length and time scales; comparison of present data with previous studies.

Stepped spillway	d_c/h (–)	Re (–)	Step edge	Y_{90} (mm)	$(L_{xz})_{\max}$ (mm)	$(T_{int})_{\max}$ (ms)	$\frac{(L_{xz})_{\max}}{d_c}$ (–)	$T_{int} \sqrt{\frac{g}{d_c}}$ (–)
$\theta = 26.6^\circ$, $h = 0.1$ m, $W = 1.0$ m	0.69	2.2×10^5	8	50.9	11.2	3.8	0.16	0.045
	0.69	2.2×10^5	9	68.7	10.6	3.2	0.15	0.038
	1.11	4.6×10^5	6	71.6	12.9	4.0	0.12	0.038
	1.11	4.6×10^5	7	70.2	13.3	3.5	0.12	0.033
	1.11	4.6×10^5	8	79.0	12.0	3.0	0.11	0.028
	1.11	4.6×10^5	9	68.4	14.7	3.3	0.13	0.031
	1.11	4.6×10^5	10	73.9	14.2	2.9	0.13	0.027
	1.28	5.7×10^5	9	88.1	15.0	3.4	0.12	0.030
	1.28	5.7×10^5	10	81.8	18.4	3.7	0.14	0.032
	1.38	6.4×10^5	10	93.4	15.0	3.1	0.11	0.026
$\theta = 26.6^\circ$, $h = 0.1$ m, $W = 0.52$ m Felder [26]	1.15	4.9×10^5	10	71.7	16.9	20.1	4.3	0.15
	1.45	6.9×10^5	10	91.0	20.1	21.2	4.0	0.14
$\theta = 26.6^\circ$, $h = 0.05$ m, $W = 1.0$ m Felder [26]	1.14	1.7×10^5	10	32.3	10.7	8.9	2.8	0.19
	2.22	4.6×10^5	16	58.9	13.1	13.8	2.7	0.12
$\theta = 21.8^\circ$, $h = 0.1$ m, $W = 1.0$ m Chanson and Carosi [21]	1.15	4.6×10^5	10	59.8	13.4	3.7	0.14	0.034
	1.45	6.4×10^5	10	73.5	16.9	3.5	0.13	0.029
$\theta = 21.8^\circ$, $h = 0.05$ m, $W = 1.0$ m Felder and Chanson [28]	1.15	1.7×10^5	10	33.4	9.3	2.6	0.18	0.034
	1.15	1.7×10^5	18	35.4	14.1	3.8	0.25	0.049
	2.39	4.9×10^5	17	69.2	15.2	2.7	0.12	0.025
	2.39	4.9×10^5	20	85.9	10.9	2.3	0.10	0.021
	3.05	6.9×10^5	20	97.8	12.6	2.3	0.09	0.019

$$\frac{L_{xz}}{(L_{xz})_{\max}} = 1.58 \times C^{0.48} \times (1 - C)^{0.27} \quad 0 \leq C \leq 1 \quad (13)$$

Table 2

Sampling parameters for sensitivity analysis; recommendation for high-velocity free surface flow measurements with phase-detection intrusive probes.

Effect of (1)	Constant parameters (2)	Effects on (3)	Outcome/recommendation (4)
Sampling frequency: 1–40 kHz	Sampling duration: 45 s	$C, F, V, Tu, (R_{xy})_{\max}, T_{xx}, T_{xy}$	Effects on a few properties → sampling frequency: 20–40 kHz
Sampling duration: 1–180 s	Sampling rate: 20 kHz	$C, F, V, Tu, (R_{xy})_{\max}, T_{xx}, T_{xy}$	No effects for 45–180 s → sampling duration 45 s
PDF-bin size: 0.05–0.1 V	Sampling duration: 45 s, sampling rate: 20 kHz	C, F	No effects for 0.05–0.1 V → PDF bin size: 0.1 V
Air–water threshold: 15–85%	Sampling duration: 45 s, sampling rate: 20 kHz	C, F	Flow region differences → 50% threshold
Sub-sample duration: 0.05–45 s	Sampling duration: 45 s, sampling rate: 20 kHz	$V, Tu, (R_{xy})_{\max}, T_{xx}, T_{xy}$	Small effects for 1–45 s → sub-sample duration: 3 s
Cut-off effect; lower cut-off 0.5 V	Sampling duration: 45 s, sampling rate: 20 kHz	$V, Tu, (R_{xy})_{\max}, T_{xx}, T_{xy}$	Large effects on Tu, T_{xx}, T_{xy} (up to 15%) → avoid cut-off

then defined as the characteristic threshold in per cent between the air–water voltage span between these two voltage peaks.

Previous investigations of the single air–water threshold identified an air–water threshold between 45% and 55% of the air–water voltage range as suitable. Toombes [50] tested the effects of thresholds between 40% and 60% of the voltage range and confirmed the findings of Herring and Davis [34] for air–water thresholds between 20% and 70%.

In the present sensitivity analysis, the effect of the air–water threshold on the void fraction and the bubble count rate was tested for thresholds between 15% and 85% (Fig. 13). Both the void fraction and bubble count rate increased slightly with increasing air–water threshold values in the bubbly flow region ($0 < C < 0.3$). For example, at location $y = 7$ mm, the bubble count rate increased from almost 30 Hz for 25% threshold to about 90 Hz for a threshold of 85% (Fig. 13). In the intermediate flow region ($0.3 < C < 0.7$), the values of both air–water properties remained almost constant for thresholds between 25% and 85%. In the spray region, the void fraction was not affected by the threshold and the bubble count rate showed a decreasing trend with increasing threshold.

The sensitivity analyses of the air–water threshold showed the significance of this parameter on the basic air–water flow properties. Depending on the threshold, the values of both air concentration and bubble frequency differed strongly especially in regions

with small air concentration. The choice of the air–water threshold is therefore essential to provide consistent results in all flow regions and for all flow situations. A choice of a threshold of 50% seems to fulfil this requirement best in high-velocity free-surface flows.

4.2. Effect of PDF bin size

The calculation of the air–water threshold is based upon the determination of the two characteristic peaks in the PDF of the raw voltage signals (Fig. 2B). A characteristic variable is the histogram bin size. A smaller bin size results in a larger amount of bins and the accuracy of the identification of the bin with the largest probability might be improved. This is important for the present voltage signals, because the maximum peaks were used for the calculation of the air–water threshold. Herein, the effect of three different bin sizes 0.01, 0.05 and 0.1 V were tested for a complete cross-section and Table 3 lists characteristic parameters comprising the equivalent clear water flow depth d , the characteristic depth Y_{90} where $C = 0.9$, the maximum bubble count rate in a cross-section F_{\max} , the corresponding air concentration $C_{F_{\max}}$, the mean air concentration C_{mean} and the depth-averaged velocity U_w . The results showed an excellent agreement for all three bin sizes indicating no effect of the bin sizes between 0.01 and 0.1 V upon the air–water flow properties.

4.3. Effect of sampling frequency

The effects of the sampling frequency on the air–water flow properties were tested for a data set recorded with sampling rate of 40 kHz for a duration of 45 s. The effects of the sampling frequencies between 1 and 40 kHz on the air–water flow properties were systematically tested. Typical results are illustrated in Fig. 14. Fig. 14A illustrates characteristic results in terms of void fraction and bubble count rate at different locations within the flow. The void fraction remained unchanged for different sampling frequencies, but the bubble count rate increased significantly with increasing sampling frequency. The results confirmed the findings of Chanson [18] in a hydraulic jump and showed that the number of bubbles was underestimated for sampling frequencies smaller than 10 kHz.

Table 3

Bin size effects of the PDF distributions of the raw voltage signal on the characteristic flow parameter in skimming flows.

Bin size (V)	d (m)	Y_{90} (m)	F_{\max} (Hz)	$Y_{F_{\max}}$ (m)	$C_{F_{\max}}$ (–)	C_{mean} (–)	U_w (m/s)
0.01	0.0571	0.0902	162.09	0.0540	0.4125	0.3669	2.9151
0.05	0.0571	0.0902	161.67	0.0540	0.4119	0.3668	2.9145
0.1	0.0571	0.0902	162.09	0.0540	0.4124	0.3668	2.9154

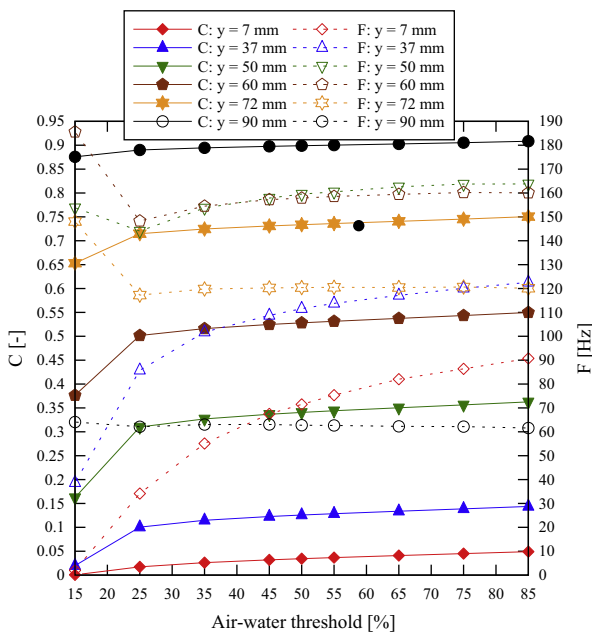


Fig. 13. Effect of the air–water threshold on the void fraction and bubble count rate; sampling rate 20 kHz, sampling duration 45 s; skimming flow data: $d_c/h = 1.38$, $q_w = 0.161 \text{ m}^2/\text{s}$, $Re = 6.4 \times 10^5$.

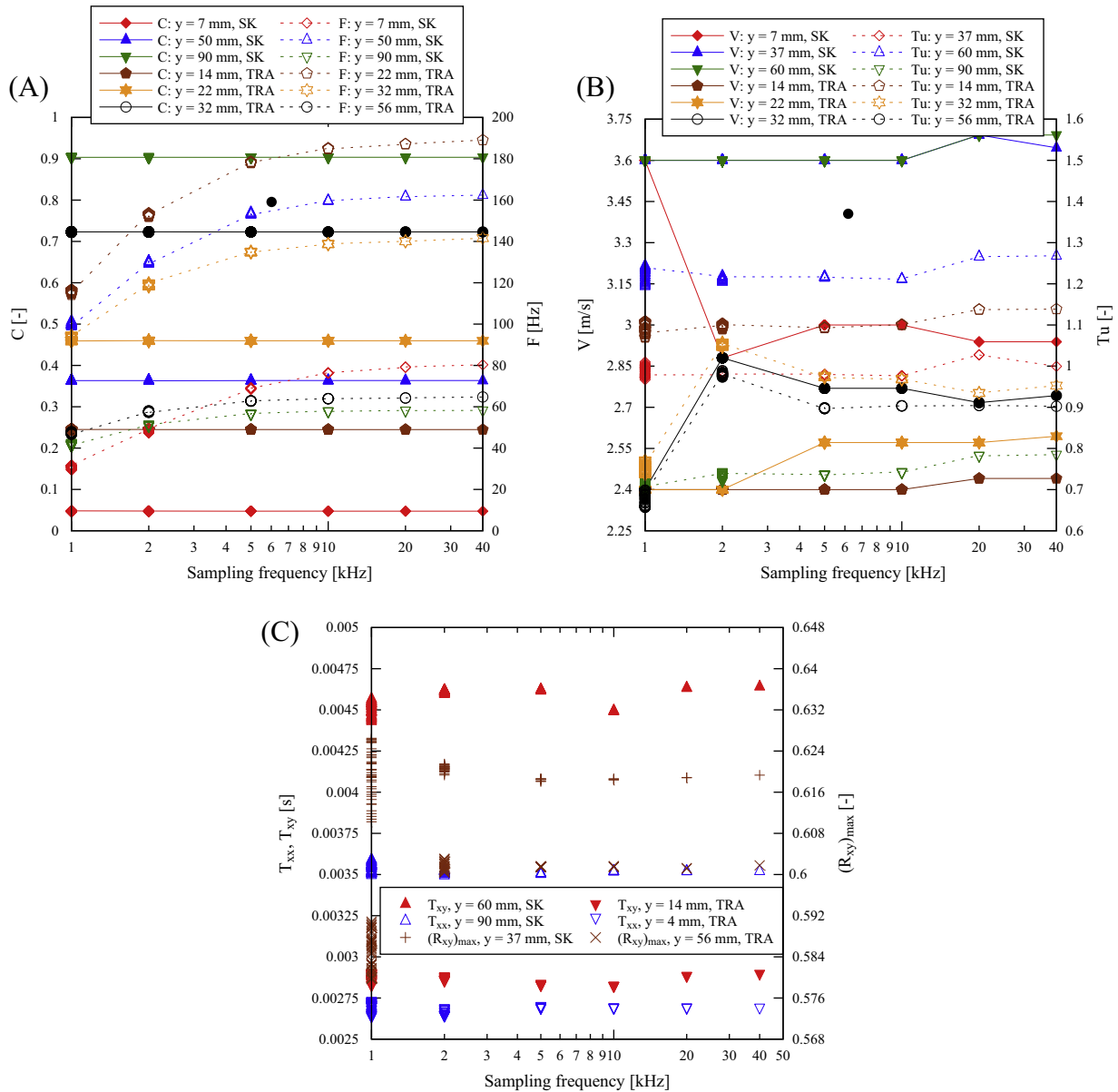


Fig. 14. Effect of sampling frequency on air-water flow properties; sampling duration 45 s, transition and skimming flow data. (A) Effect on time-averaged void fraction and bubble count rate. (B) Effect on interfacial velocity and turbulence intensity. (C) Effect on correlation time scales and maximum cross-correlation coefficient.

The effects of sampling frequency on the interfacial velocity and turbulence intensity are illustrated in Fig. 14B. For most flow regions in transition and skimming flows, the velocity remained almost constant for sampling frequencies larger 5 kHz with slightly larger velocities for frequencies of 20 kHz and 40 kHz. The turbulence intensities confirmed this trend and large scatter of data could be seen for small frequencies. Small discrepancies in the turbulence data suggest a high sampling frequency of 20–40 kHz for most accurate results.

Typical results in terms of auto- and cross-correlation time scales and the maximum cross-correlation coefficient are illustrated in Fig. 14C. For the flow properties, large scatter was visible for sampling rates smaller 5 kHz. The most consistent results were visible for 20 and 40 kHz. However the differences in time scales and maximum cross-correlation coefficients were small and the effect of the sampling frequency was negligible compared to the effect on the bubble count rate, interfacial velocity and turbulence intensity.

Overall, the present observations suggested best results for frequencies larger than 10–20 kHz. A larger sampling rate of 40 kHz would yield almost identical results, but the amount of recorded data would be larger.

4.4. Effect of sampling duration

Another fundamental parameter is the sampling duration. Toombes [50] showed that the sampling period has significant effects on the void fraction and bubble count rate and identified a sampling time of at least 10 s as sufficient for his experiments on a stepped spillway. André et al. [1] investigated the effects of sampling duration upon the interfacial velocity and the cross-correlation coefficient and suggested a sampling duration of more than 30 s. On a hydraulic jump, Chanson [18] showed no effects of sampling durations larger 30–40 s for bubble count rate and void fraction.

In the present investigation, an analysis was conducted for sampling durations between 1 and 180 s with a sampling frequency of 20 kHz per sensor in both skimming and transition flows (Fig. 15). In Fig. 15A, characteristic observations of void fraction and bubble frequency are shown highlighting increasing data scatter with decreasing sampling duration. Fig. 15A showed that the sampling rate had little effect on void fraction and bubble frequency for sampling periods larger 45 s.

Similar results were found for the other air–water flow properties. In Fig. 15B, it is visible that the sampling duration had significant influence on the interfacial velocity and the turbulence intensity. Fig. 15C illustrates even stronger scatter in terms of the maximum cross-correlation and the auto- and cross-correlation time scales for sampling durations smaller 45 s. The sampling duration had large effects on the auto- and cross-correlation analyses of the raw signals. With decreasing sampling duration, the amount of raw data points became too small for accurate observations. Therefore a sampling rate of at least 45 s is required for a sampling frequency of 20 kHz. For higher sampling frequencies, the required sampling duration might be smaller.

4.5. Effect of sub-sample duration

The calculation of some air–water flow properties is based on statistical analyses of the raw signals of the conductivity probe. For a double tip probe, the auto- and cross-correlation analyses of the leading and trailing tips are typically used to calculate the maximum cross-correlation, the interfacial velocity, the turbulence intensity u and the auto- and cross-correlation time scales. For large data sets, the resolution of the auto- and cross-correlation functions can be biased inversely proportional to the amount of data [32] and the air–water flow properties might be adversely affected.

A test of different sub-sample durations between 0.05 and 45 s was performed for experimental measurements conducted for 45 s with a sampling frequency of 20 kHz. Typical results for both transition and skimming flows are illustrated in Fig. 16. For sub-sample durations between 1 and 45 s, the maximum cross-correlation coefficient did not change significantly and decreased for smaller sub-sample durations. The interfacial velocities were identical for all sub-sample durations and for all locations in both skimming

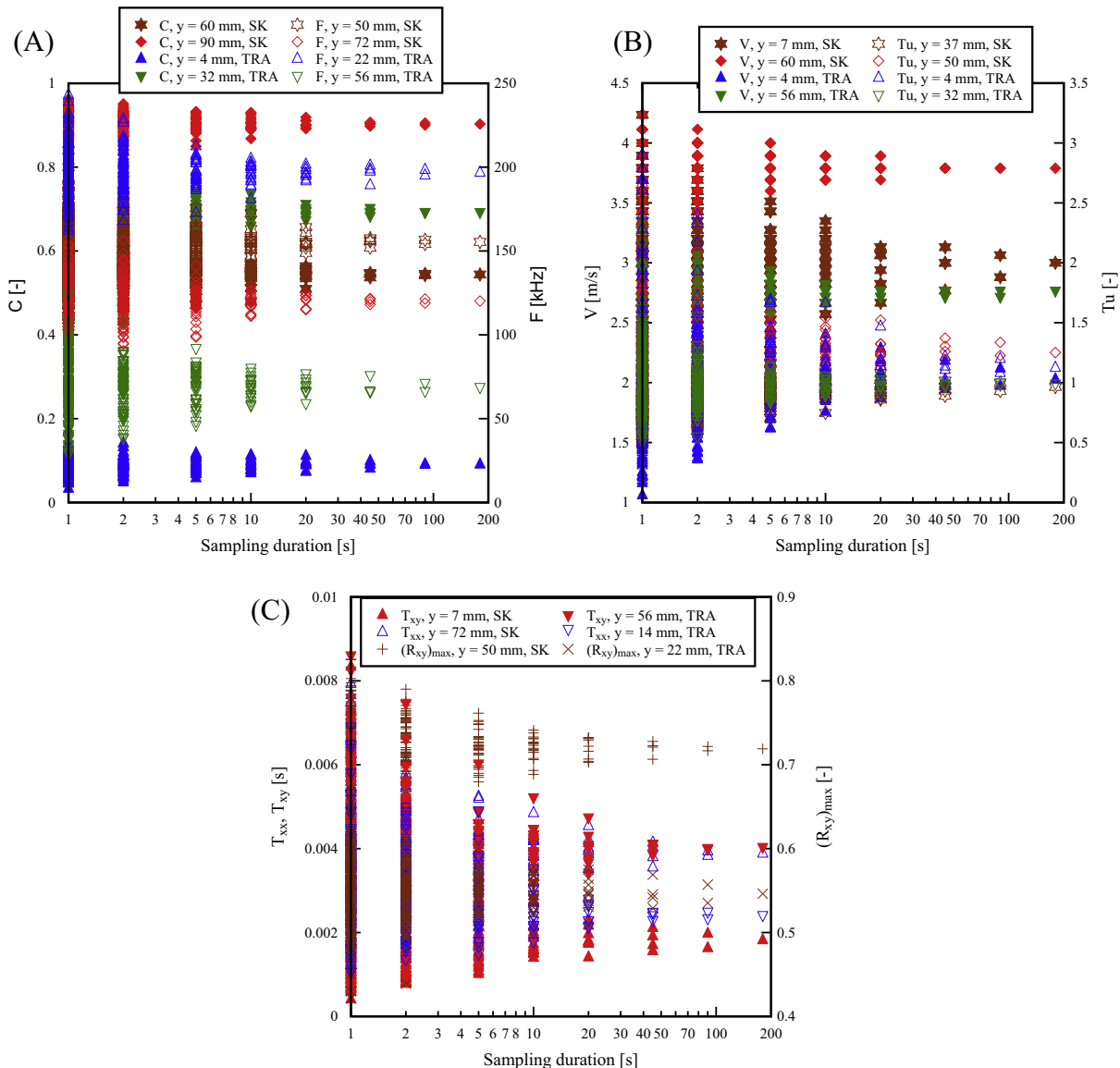


Fig. 15. Effect of sampling duration on air–water flow properties; sampling frequency 20 kHz, transition and skimming flow data. (A) Effect on time-averaged void fraction and bubble count rate. (B) Effect on interfacial velocity and turbulence intensity. (C) Effect on correlation time scales and maximum cross-correlation coefficient.

and transition flows (not illustrated). The turbulence intensity and the auto- and cross-correlation time scales decreased consistently with decreasing sub-sample duration with a sharpest decline for sub-sample duration smaller than 1 s (Fig. 16). This effect was linked with the smaller number of detected bubbles in the sub-sample segments.

The results of the sub-sample duration sensitivity analysis suggest that a sub-sample duration must be larger than 1 s. Considering the correlation of large data sets might be biased, the largest sub-sample durations might yield an overestimation of the air–water flow properties. It seems most appropriate to use a sub-sample duration of 3–5 s (i.e. an ensemble averaging of 15–9 segments) for the analyses of the experimental data as most robust for the air–water flow column.

4.6. Cut-off effects of air voltage signals

A further sensitivity analysis was conducted to investigate the cut-off effects for air voltage signals on the air–water flow properties. The principle of the conductivity probes is based on the different resistivity of water and air with larger resistivity of air compared to water. Larger voltage signals around 4 V correspond to a water phase (Fig. 2). The voltage raw signal of air is much smaller of about 0.5 V. For both signals some voltage noise was present and the voltage signals fluctuated around their two characteristic peak voltages (Fig. 2). The effect of a constant lower voltage cut-off was tested. Every time the voltage signal was smaller than 0.5 V, it was replaced by the constant 0.5 V, i.e. smaller values were cut-off from the statistical data processing. The effects of this lower constant cut-off were analysed for the interfacial velocity, turbulence intensity, maximum cross-correlation coefficient and auto- and cross-correlation time scales (Table 4).

The comparative results showed that there were no differences in the interfacial velocities and small differences in the maximum cross-correlation values. For the turbulence intensity and the auto- and cross-correlation time scales, the effects were larger with differences of up to 15% in the spray region (Table 4). The deviations between the air–water flow properties of the two data sets increased with increasing void fraction. The cut-off of raw voltage signals should be avoided.

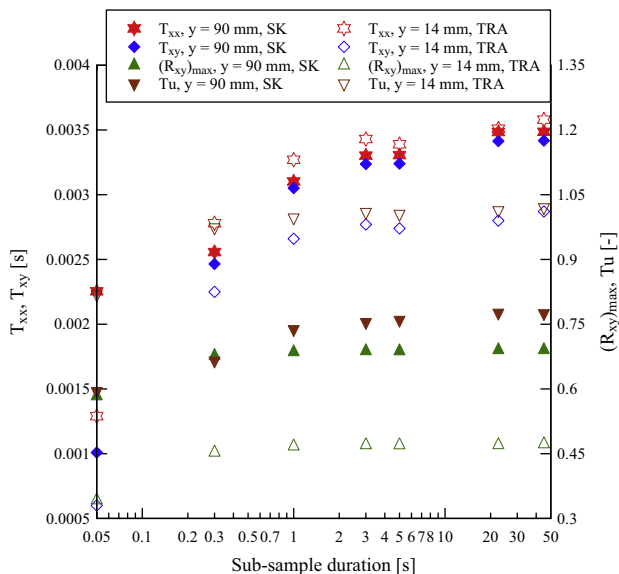


Fig. 16. Sensitivity analysis on the effect of sub-sample duration on the correlation time scales, the maximum cross-correlation coefficient and the turbulence intensity; sampling duration 45 s, sampling frequency 20 kHz, transition and skimming flow data.

Table 4

Effects of the lower cut-off of 0.5 V on some air–water flow properties in skimming flows.

	Cut-off	V (m/s)	Tu (–)	T_{xx} (s)	T_{xy} (s)	$(R_{xy})_{max}$ (–)
$y = 90$ mm	No	3.7436	0.7546	0.0033	0.0032	0.6880
$y = 90$ mm	Yes	3.7436	0.6947	0.0028	0.0027	0.6719
$y = 72$ mm	No	3.7436	1.0243	0.0038	0.0038	0.7108
$y = 72$ mm	Yes	3.7436	0.9664	0.0035	0.0034	0.7016
$y = 60$ mm	No	3.8421	1.3110	0.0045	0.0045	0.7153
$y = 60$ mm	Yes	3.8421	1.2633	0.0043	0.0044	0.7103

5. Conclusions

Air–water flow experiments were conducted with phase-detection conductivity probes on a large size stepped spillway model with slope of 26.6°. The experiments covered two sub-regimes of the free-surface air–water flows, i.e. transition and skimming flows. The study provided a comprehensive analysis of the full range of air–water flow properties for both flow regimes including the basic air–water flow parameters as well as the turbulent properties. The comparison of transition and skimming flow data highlighted differences for the transition flow regime between adjacent step edges linked to instable air–water flow processes. Despite these differences the present data showed a close agreement in terms of large scale turbulent structures within the air–water flows and the self-similarity of turbulent data in both flow regimes.

Furthermore a sensitivity analysis was conducted to identify optimum sampling and signal processing parameters for phase-detection intrusive probe measurements in high-velocity free-surface flows. For the present investigation of the full set of air–water flow properties, a sampling duration of 45 s, a sampling rate of 20 kHz, a sub-sample duration of 3 s and an air–water threshold of 50% was optimum for the full air–water flow column. Air–water flow experiments with phase-detection probes should be conducted with at least 900,000 measurement points. The present sensitivity analyses provided a sampling procedure for high-velocity air–water flow experiments with phase-detection intrusive probes including a recommendation for particular sampling parameters depending upon the investigated air–water flow properties. The present results suggested that the sampling parameters could be applied for further free-surface air–water flows such as on smooth spillways and jets. The application to air–water flows in hydraulic jumps and drop shafts might be also possible.

Acknowledgment

The financial support of the Australian Research Council (Grants DP0818922 and DP120100481) is acknowledged.

References

- [1] S. André, J.L. Boillat, A.J. Schleiss, Two-phase flow characteristics of stepped spillways. discussion, *J. Hydraul. Eng. ASCE* 131 (2005) 423–427.
- [2] W.D. Bachalo, Experimental methods in multiphase flows, *Int. J. Multiph. Flow* 20 (1994) 261–295.
- [3] F.A. Bombardelli, Computational multi-phase fluid dynamics to address flows past hydraulic structures. In: 4th IAHR Intl. Symp. Hydraulic structures, APRH, Porto, Portugal, 9–11, February 2012.
- [4] R.M. Boes, Zweiphasenströmung und Energieumsetzung an Grosskaskaden. (Two-Phase Flow and Energy Dissipation on Cascades.) PhD Thesis, VAW-ETH, Switzerland, 2000.
- [5] C. Boyer, A.M. Duquenne, G. Wild, Measuring techniques in gas–liquid and gas–liquid–solid reactors, *Chem. Eng. Sci.* 57 (2002) 3185–3215.
- [6] D.B. Bung, Zur selbstbelüfteten Gerinneströmung auf Kaskaden mit gemäßigter Neigung. PhD Thesis, Lehr- und Forschungsgebiet Wasserwirtschaft und Wasserbau, Bergische Universität Wuppertal, Germany, 2009.
- [7] P. Cain, I.R. Wood, Instrumentation for aerated flow on spillways, *J. Hyd. Div. ASCE* 107 (1981) 1407–1424.

- [8] P. Cain, I.R. Wood, Measurements of self-aerated flow on a spillway, *J. Hyd. Div. ASCE* 107 (1981) 1425–1444.
- [9] G. Carosi, H. Chanson, Turbulence characteristics in skimming flows on stepped spillways, *Can. J. Civil Eng.* 35 (2008) 865–880.
- [10] A. Cartellier, Simultaneous void fraction measurement, bubble velocity, and size estimate using a single optical probe in gas-liquid two-phase flows, *Rev. Sci. Instrum.* 63 (1992) 5442–5453.
- [11] A. Cartellier, J.L. Achard, Local phase detection probes in fluid/fluid two-phase flows, *Rev. Sci. Instrum.* 62 (1991) 279–303.
- [12] A. Cartellier, E. Barrau, Monofiber optical probes for gas detection and gas velocity measurements: conical probes, *Int. J. Multiph. Flow* 24 (1998) 1265–1294.
- [13] M.R. Chamani, N. Rajaratnam, Characteristics of skimming flow over stepped spillways, *J. Hydraul. Eng. ASCE* 125 (1999) 361–368.
- [14] H. Chanson, A study of Air Entrainment and Aeration Devices on a Spillway Model. PhD Thesis, University of Canterbury, New Zealand, 1988.
- [15] H. Chanson, Air Bubble Entrainment in Free-Surface Turbulent Shear Flows, Academic Press, London, 1997. p. 401.
- [16] H. Chanson, Air-water flow measurements with intrusive phase-detection probes. Can we improve their interpretation?, *J. Hydraul. Eng. ASCE* 128 (2002) 252–255.
- [17] H. Chanson, Bubbly flow structure in hydraulic jump, *Eur. J. Mech. B-Fluid* 26 (2007) 367–384.
- [18] H. Chanson, Dynamic similarity and scale effects affecting air bubble entrainment in hydraulic jumps. In: 6th Intl. Conf. Multiphase Flow, ICMF, Leipzig, Germany, 9–13, July 2007.
- [19] H. Chanson, Hydraulics of aerated flows: qui pro quo?, *J. Hydraul. Res. IAHR* 51 (2013) 223–243, <http://dx.doi.org/10.1080/00221686.2013.795917>.
- [20] H. Chanson, G. Carosi, Advanced post-processing and correlation analyses in high-velocity air–water flows, *Environ. Fluid Mech.* 7 (2007) 495–508, <http://dx.doi.org/10.1007/s10652-007-9038-3>.
- [21] H. Chanson, G. Carosi, Turbulent time and length scale measurements in high-velocity open channel flows, *Exp. Fluids* 42 (2007) 385–401, <http://dx.doi.org/10.1007/s00348-006-0246-2>.
- [22] H. Chanson, L. Toombes, Air–water flows down stepped chutes: turbulence and flow structure observations, *Int. J. Multiph. Flow* 28 (2002) 1737–1761.
- [23] H. Chanson, L. Toombes, Hydraulics of stepped chutes: the transition flow, *J. Hydraul. Res. IAHR* 42 (2004) 43–54.
- [24] C. Crowe, M. Sommerfeld, Y. Tsuji, *Multiphase Flows with Droplets and Particles*, CRC Press, Boca Raton, USA, 1998. 471p.
- [25] P.D. Cummings, Aeration due to Breaking Waves. PhD Thesis, The University of Queensland, Australia, 1996.
- [26] S. Felder, Air–Water Flow Properties on Stepped Spillways for Embankment Dams: Aeration, Energy Dissipation and Turbulence on Uniform, Non-Uniform and Pooled Stepped Chutes. PhD Thesis, The University of Queensland, Australia, 2013.
- [27] S. Felder, H. Chanson, Turbulence and turbulent length and time scales in skimming flows on a stepped spillway. Dynamic similarity, physical modelling and scale effects. Report CH64/07, Division of Civil Engineering, The University of Queensland, Brisbane, 2008, 217p.
- [28] S. Felder, H. Chanson, Turbulence, dynamic similarity and scale effects in high-velocity free-surface flows above a stepped chute, *Exp. Fluids* 47 (2009) 1–18.
- [29] S. Felder, H. Chanson, Air–water flow properties in step cavity down a stepped chute, *Int. J. Multiph. Flow* 37 (2011) 732–745.
- [30] S. Felder, H. Chanson, Triple Decomposition Technique in Air–Water Flows: Application to Stationary Flows on a Stepped Spillway, *Int. J. Multiph. Flow* 58 (2014) 139–153, <http://dx.doi.org/10.1016/j.ijmultiphaseflow.2013.09.006>.
- [31] K.W. Frizell, F.M. Renna, Laboratory studies on the cavitation potential of stepped spillways. In: 34th IAHR World Congress, Brisbane, Australia, 26 June–1 July 2011, pp. 2420–2427.
- [32] M.H. Hayes, *Statistical Digital Signal Processing and Modeling*, John Wiley, New York, USA, 1996. 624p.
- [33] R.A. Herringe, A Study of the Structure of Gas-Liquid Mixture Flows. PhD Thesis, University of New South Wales, Australia 1973.
- [34] R.A. Herringe, M.R. Davis, Detection of instantaneous phase changes in gas–liquid mixtures, *J. Phys. E* 7 (1974) 807–812.
- [35] R.A. Herringe, M.R. Davis, Structural development of gas–liquid mixture flows, *J. Fluid Mech.* 73 (1976) 97–123.
- [36] S.L. Hunt, K.C. Kadavy, Energy dissipation on flat-sloped stepped spillways: Part 1. Upstream of the inception point, *Trans. ASABE* 53 (2010) 103–109.
- [37] O.C. Jones, J.M. Delhaye, Transient and statistical measurement techniques for two-phase flows: a critical review, *Int. J. Multiph. Flow* 3 (1976) 89–116.
- [38] H. Kipphan, Bestimmung von Transportkenngrößen bei Mehrphasenströmungen mit Hilfe der Korrelationsmeßtechnik. (Determination of Transport Parameters in Multiphase Flow with Aid of Correlation Measuring Technique.), *Chem. Ing. Technol.* 49 (1977) 695–707 (in German).
- [39] J. Matos, Onset of skimming flow on stepped spillways. Discussion, *J. Hydraul. Eng. ASCE* 127 (2001) 519–521.
- [40] F. Murzyn, H. Chanson, Experimental investigation of bubbly flow and turbulence in hydraulic jumps, *Environ. Fluid Mech.* 9 (2009) 143–159.
- [41] F. Murzyn, D. Mouaze, J.R. Chaplin, Optical fibre probe measurements of bubbly flow in hydraulic jumps, *Int. J. Multiph. Flow* 31 (2005) 141–154.
- [42] L.S. Neal, S.G. Bankoff, A high resolution resistivity probe for determination of local void properties in gas–liquid flows, *Am. Inst. Chem. J.* 9 (1963) 49–54.
- [43] L.S. Neal, S.G. Bankoff, Local parameters in cocurrent mercury–nitrogen flow, *Am. Inst. Chem. J.* 11 (1965) 624–635.
- [44] S. Pagliara, T. Roshni, I. Carnacina, Aeration and velocity profile over block ramp elements. In: 33rd IAHR congress, Vancouver, BC, Canada, 9–14, August 2009.
- [45] N.S.L. Rao, H.E. Kobus, Characteristics of self-aerated free-surface flows, *Water and Waste Water/Current Research and Practice*, vol. 10, Eric Schmidt Verlag, Berlin, Germany, 1971.
- [46] N. Rajaratnam, Skimming Flow in Stepped Spillways, *J. Hydraul. Eng.* 116 (4) (1990) 587–591.
- [47] A. Serizawa, I. Kataoka, I. Michiyoshi, Turbulence structure of air–water bubbly flows – I. Measuring techniques, *Int. J. Multiph. Flow* 2 (1975) 221–233.
- [48] M. Takahashi, I. Ohtsu, Aerated flow characteristics of skimming flow over stepped chutes, *J. Hydraul. Res. IAHR* 50 (2012) 427–434.
- [49] M. Takahashi, C.A. Gonzalez, H. Chanson, Self-Aeration and Turbulence in a Stepped Channel: Influence of Cavity Surface Roughness, *Int. J. Multiph. Flow* 32 (12) (2006) 1370–1385, <http://dx.doi.org/10.1016/j.ijmultiphaseflow.2006.07.001>.
- [50] L. Toombes, Experimental Study of Air–Water Flow Properties on Low-Gradient Stepped Cascades. PhD Thesis, The University of Queensland, Australia, 2002.
- [51] A. Tricia, C.H. Waniowski, C.E. Brennen, Bubble measurements downstream of hydraulic jumps, *Int. J. Multiph. Flow* 27 (2001) 1271–1284.
- [52] I.R. Wood, Air Entrainment in Free-surface Flows: IAHR Hydraulic Structures Design Manual no. 4, Hydraulic Design Considerations, Balkema, Rotterdam, 1991.